ADVANCED MATERIALS TECHNOLOGIES
www.advmattechnol.de

# A Bioinspired Plasmonic Nanocomposite Actuator Sunlight-Driven by a Photothermal-Hygroscopic Effect for Sustainable Soft Robotics

*Stefano Mariani,* Luca Cecchini, Alessio Mondini, Emanuela Del Dottore, Marilena Ronzan, Carlo Filippeschi, Nicola Maria Pugno, Edoardo Sinibaldi,* and Barbara Mazzolai**

**Combined photothermal-hygroscopic effects enable novel materials actuation strategies based on renewable and sustainable energy sources such as sunlight. Plasmonic nanoparticles have gained considerable interest as photothermal agents, however, the employment in sunlight-driven photothermal-hygroscopic actuators is still bounded, mainly due to the limited absorbance once integrated into nanocomposite actuators and the restricted plasmonic peaks amplitude (compared to the solar spectrum). Herein, the design and fabrication of an AgNPs-based plasmonic photothermal-hygroscopic actuator integrated with printed cellulose tracks are reported (bioinspired to Geraniaceae seeds structures). The nanocomposite is actuated by sunlight power density (i.e., 1 Sun = 100 mW cm$^{-2}$). The plasmonic AgNPs are in situ synthesized on the PDMS surface through a one-step and efficient fluoride-assisted synthesis (surface coverage ≈40%). The nanocomposite has a broadband absorbance in the VIS range (>1) and a Photothermal Conversion Efficiency ≈40%. The actuator is designed exploiting a mechanical model that predicted the curvature and forces, featuring a ≈6.8 ± 0.3 s response time, associated with a ≈43% change in curvature and a 0.76 ± 0.02 mN force under 1 Sun irradiation. The plasmonic nanocomposite actuator can be used for multiple tasks, as hinted through illustrative soft robotics demonstrators, thus fostering a bioinspired approach to developing embodied energy systems driven by sunlight.**

## 1. Introduction

Soft material systems, and in particular soft robots, actioned by environmental energy sources offer great potential for developing sustainable robotics and environmental applications.[1–4]

In this regard, Nature offers priceless sources of inspiration, including many plants and seeds that adaptively leverage environmental stimuli, including humidity and sunlight, to effectively move and interact with their ecosystems.[5–9]

For example, pinecones,[5,6] wheat,[7] and Geraniaceae seed structures[8] adsorb water molecules (from environmental moisture) onto locally-aligned hygroscopic cellulose-based microstructures in the cells, thus enacting shape changes functional to lifecycle tasks (e.g., opening/close in pinecones[5,6] and locomotion in wheat and Geraniaceae seeds),[7,8] aimed at seeds dispersal and germination.

Complementarily, juvenile sunflower plants track the Sun's movement thanks to the circadian rhythms that regulate

S. Mariani, L. Cecchini, A. Mondini, E. Del Dottore, M. Ronzan, C. Filippeschi, E. Sinibaldi, B. Mazzolai
Bioinspired Soft Robotics Laboratory
Istituto Italiano di Tecnologia
Via Morego 30, Genova 16163, Italy
E-mail: stefano.mariani@iit.it; edoardo.sinibaldi@iit.it; barbara.mazzolai@iit.it

L. Cecchini, N. M. Pugno
Laboratory for Bioinspired
Bionic
Nano
Meta Materials and Mechanics
Department of Civil
Environmental and Mechanical Engineering
University di Trento
Via Mesiano 77, Trento 38123, Italy

N. M. Pugno
School of Engineering and Materials Science
Queen Mary University of London
Mile End Road, London E1 4NS, United Kingdom

The ORCID identification number(s) for the author(s) of this article can be found under https://doi.org/10.1002/admt.202202166



**DOI: 10.1002/admt.202202166**

the east-west asymmetric elongation of cells modulated by the auxin signaling pathway, thereby enhancing plant growth and pollinator visits to the flowers.[9]

Overall, Plants and seeds offer a wide range of actuation mechanisms with energy consumption powered by environmental stimuli.

For this reason, artificial actuation systems inspired by plants have been proposed, with growing interest, in stimuli-responsive material through hygroscopic actuation. In this regard, moisture-responsive multilayers, capable of bending upon exposure to humidity, based on the differential geometric, mechanical, and hygroscopic properties of the involved layers, have been investigated.[10–15]

Differently, light-responsive actuators have been mostly studied by focusing on specific material properties as well as *trans–cis* isomerization (e.g., in azobenzene-based molecules)[16] or photothermal conversion[17,18] (e.g., in MXenes,[19–22] Graphene,[23–25] Carbon Nanotubes (CNTs)[26] and Metal Nanoparticles (MNPs).[27–32]

In general, once photoexcitation converts into heat, multiple transduction pathways can be implemented to achieve actuation, e.g., through thermal expansion/contraction, water adsorption/desorption, phase change, and modulation of the physicochemical properties of the involved (nano) composites, and additional effects such as, e.g., the creation of surface tension gradients.[18] Finally, some efforts have been devoted to the use of photothermal conversion to induce reversible water adsorption/desorption, thus coupling photothermal and hygroscopic approaches to achieve reversible actuation.[18–21,24,25]

However, photothermal-humidity driven actuation in multilayered structures based on non-coherent and low-power-density light sources, as provided by ordinary solar radiation (e.g., UV–Vis radiation with a power density of 1 Sun = 100 mW $cm^{-2}$), is highly requested to exploit such a ubiquitously available natural power source. This could effectively open new avenues for sustainable actuation strategies, but it still poses a tremendous challenge.

Examples of photothermal-hygroscopic driven actuation at power densities comparable to solar radiation rely on the integration of high Photothermal Conversion Efficiency (P.C.E.) materials based on Carbon (e.g., CNT and graphene)[18] (P.C.E ≈ 80%–90%) and MXene (P.C.E.≈100%).[20,33]

Despite the high P.C.E., integration of these materials into sunlight-driven actuators introduces several issues. For instance, MXene requires long (48 h) synthesis and elaborated purification and functionalization steps.[19,20] Moreover, MXene, graphene, and CNTs are usually ex-situ integrated[19,20] in the nanocomposites.

Alternatively, thermoplasmonic metal nanoparticles (MNPs) with localized surface plasmon resonances (LSPR) have gained considerable interest due to their ability to manipulate light from solar energy at the nanometer scale and convert it into heat for energetically sustainable development purposes.[34] However, the applications in photothermal-hygroscopic actuators, driven by only sunlight, are still to be demonstrated due to the relatively restricted LSPR peaks amplitude (compared to the solar spectrum amplitude) and the poor functionalization yield in nanocomposite materials.

Here we report the first fully NPs-based plasmonic and photothermal-hygroscopic actuator driven by sunlight. Specifically, a trilayer structure was implemented, with a PDMS base layer (BL) for structural support upon that a nanometric middle AgNPs layer (Plasmonic Photothermal Layer, PPTL) was synthesized for exploiting heat generation upon solar radiance, and an upper anisotropically hygroscopic layer (HL), based on cellulose, devised to finally transduce actuation through bending.

As regards the photothermal mechanism, the AgNPs were synthesized by adapting a single-step, in situ, and fluoride-assisted synthesis reduction protocol recently disclosed by Mariani et al.,[35,36] only using the PDMS layer (as reducing agent) and AgF in ethanolic solution. Such a novel synthesis allowed the achievement of high-yield surface coverage (40%) of AgNPs firmly anchored to the PDMS surface, with broadband and high absorption value in the visible range (>1) and a P.C.E. ≈40% under 1 Sun irradiation (100 mW $cm^{-2}$).

As regards the hygroscopic mechanism, aligned tracks of hygroscopic carboxymethyl cellulose (CMC) were printed on the BL/PPTL actuator by taking inspiration from the Geraniaceae seed structure of *Pelargonium appendiculatum* (L.fil.) Willd. Since cellulose materials have a hygroscopic and water-swelling nature thanks to the abundant hydrophilic groups, we adopted CMC because it is an anionic charged cellulose derivative with a more pronounced water-swelling ratio than native cellulose.[37]

Thanks to the photothermal effect of AgNPs, the loss of humidity induced in the CMC enacts actuation, with strong curvature changes (over 40%) in a short response time ($6.8 \pm 0.3$ s) and a force generation of $0.76 \pm 0.02$ mN under 1 Sun irradiation.

A purposively theoretical model predicted the kinematics and the statics under controlled humidity exposure.[38]

Moreover, crawling, coiling/rolling, gripping, and weightlifting capabilities were also demonstrated for a rectangular actuator, as well as shape reconfiguration illustrated by implementing the trilayer into an actuator devised for programmed motion responsive to sunlight.

The achieved results disclose the possibility of using sunlight to drive photothermal-hygroscopic actuators based only on plasmonic MNPs as photothermal agents. Besides avoiding the criticalities associated with actuator implementations based on MXene, graphene, and CNT, while also matching the related performance in terms of light power densities vs response times (few seconds) (Figure S1, Supporting Information), the obtained results pave the way for a novel class of hygroscopic soft actuators driven by natural environmental conditions, thus fostering the energetically sustainable development of soft material, actuators, and robots.

## 2. Results and Discussions

**Figure 1**a and Figure S2 (Supporting Information) illustrate the fabrication of the plasmonic photothermal-hygroscopic nanocomposites consisting in: 1) PDMS preparation (Base Layer, BL); 2) in situ synthesis of plasmonic AgNPs exploiting a recent and high yield fluoride-assisted techniques developed by Mariani et al.,[35,36] (Plasmonic Photothermal Layer, PPTL); CMC printing using Direct Ink Writing (Video S1, Supporting Information) (Hygroscopic Layer, HL). The multilayered structure

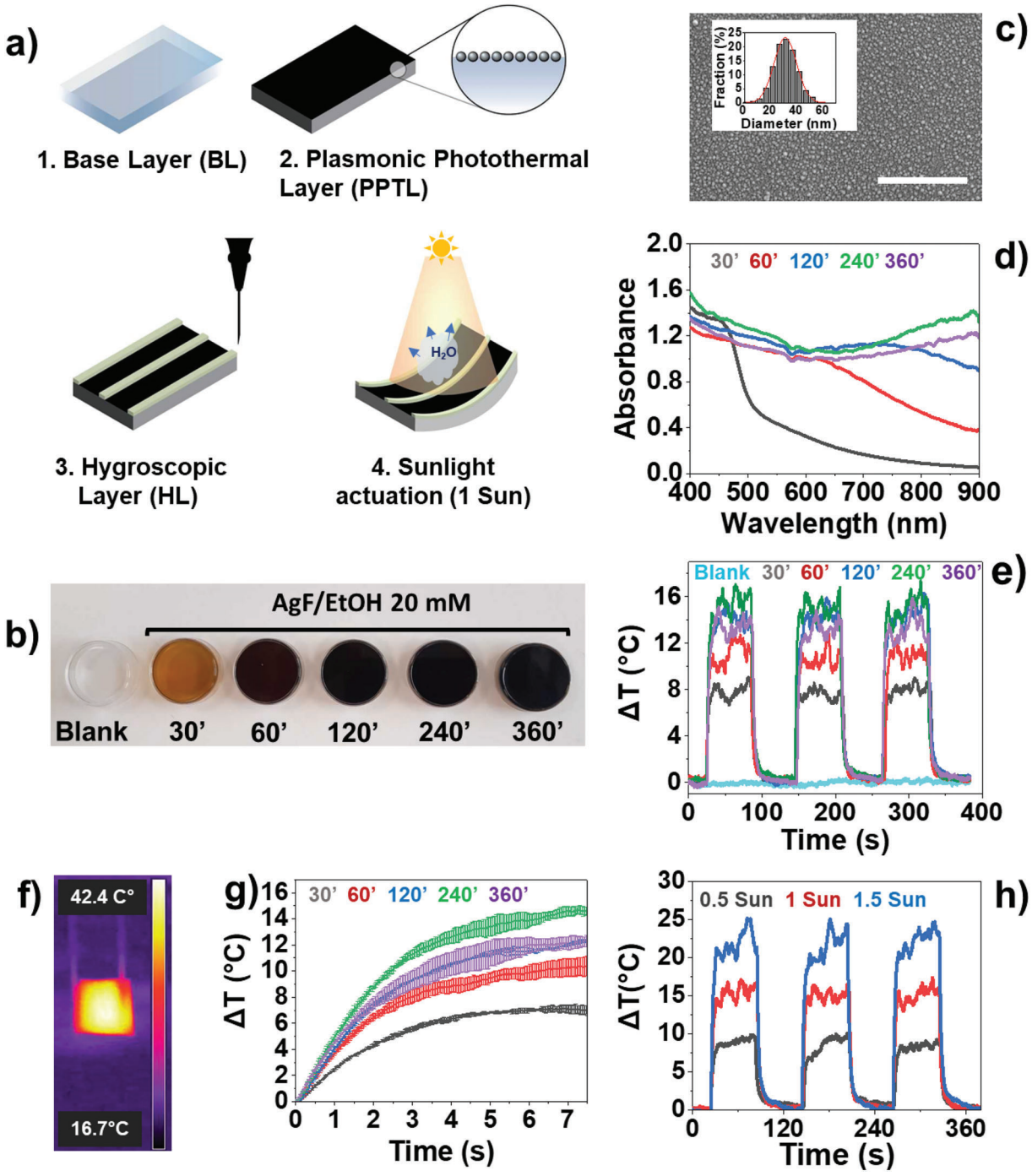


**Figure 1.** a) Fabrication sketch of the photothermal-hygroscopic actuator consisting of: 1. PDMS preparation (Base Layer, BL); 2. In situ synthesis of plasmonic AgNPs through a fluoride-assisted method (Plasmonic Photothermal Layer, PPTL); 3. Carboxymethyl Cellulose (CMC) printing on PPTL through Direct Ink Writing (DIW) (Hygroscopic Layer, HL); 4. Photothermal-hygroscopic actuation under 1 Sun. b) Pictures of PDMS prepared in Petri dishes and decorated with AgNPs in a fluoride solution (i.e., 20 mM AgF) for 30–360 min. c) SEM image of the PDMS surface decorated with AgNPs for 240 min. Scalebar is 1 μm. In the inset is reported the AgNPs distribution. d) Absorbance spectra of PDMS decorated with AgNPs reported in (b). e) Temperature variations (ΔT,°C) over time on the PDMS/AgNPs samples reported in (b) and exposed to a solar simulator light with a power density of 100 mW $cm^{-2}$ with intermitting solar irradiation (60 s irradiation/60 s of darkness). f) Photothermal camera image of the PDMS surface decorated with AgNPs for 240 min and exposed to a solar simulator light with a power density of 100 mW $cm^{-2}$. The thermal color scale shows the maximum and minimum temperature values recorded in the image. g) Synchronized temperature variations (ΔT,°C) over time on the PDMS/AgNPs samples reported in (b) and exposed to a solar simulator light with a power density of 100 mW $cm^{-2}$. Data are provided as average values over 3 replicates with error bars representing one standard deviation. h) Temperature variations (ΔT,°C) over time on the PDMS sample with AgNPs decorated for 240 min and exposed to solar simulator light with different power densities of 50, 100, and 150 mW $cm^{-2}$ (0.5, 1, and 1.5 Sun) and with intermitting solar irradiation (60 s irradiation/60 s) of darkness.

BL/PPTL/HL was actuated by photothermal-hygroscopic effect under 1 Sun irradiation.

The thickness of the PDMS (BL) was 49 ± 4 µm (N samples = 8) (Figure S3, Supporting Information). AgNPs were formed on the PDMS adapting the one-step and in situ redox reaction occurring between unreacted Si–H bonds of the curing agent and $Ag^+$ available in the ethanolic AgF solution. The fluoride ions in the metal solution improved density and accelerated the kinetics of the synthetic process with respect to state-of-the-art fluoride-free approaches.[35]

Figure 1b shows both blank PDMS (not decorated, BL) and PDMS decorated with AgNPs by casting 20 mM AgF ethanolic solutions for different times (PPTL), namely from 30 to 360 min. PDMS showed from brownish to black color intensities increasing with the decoration time.

This effect is ascribable to Localized Surface Plasmon Resonance (LSPR) cumulative absorption of the formed NPs, which increase both in size[39] and distribution, combined with a plasmonic interparticle coupling as previously reported both for AgNPs (adsorbed onto solid surfaces)[40] and AuNPs in liquid solutions.[41]

SEM analysis of the PDMS petri decorated in ethanolic solutions of AgF at 60, 120, 240, and 360 min is reported in Figure 1c and Figure S4 (Supporting Information). SEM EDX analysis reported in Figure S5 (Supporting Information), for the AgNPs synthesis of 240 min, shows the appearance of a strong Ag signal (Weight% = 63.88 ± 0.35%) due to the in situ synthesis. It is interesting to note that the oxygen signal (due to Si–O–Si bonding in the PDMS structure) is higher (Weight% = 11.26 ± 0.58%) compared to the expected one (Weight% = 9.28%) and this is due to the oxidation of the silicon during the in situ redox reaction as reported in[42,43].

The AgNPs average sizes increased from 21 to 35 nm as the decoration time increased from 60 to 360 min. All the NPs distributions were well fitted by Gaussian profiles ($R^2$ = 0.99) (Figure S6a–e, Supporting Information).

The surface coverage of the AgNPs was 23.31%, 40.36%, 40.72%, and 41.02%, for 60, 120, 240, and 360 min of decoration, respectively Figure S6f (Supporting Information).

We monitored the decoration process by using absorption spectroscopy (Figure 1d) after the measurement of the reflectance and transmittance spectra in the visible range (400–900/1000 nm) (Figure S7a–c, Supporting Information) given that the sunlight simulator has significant irradiance values only between 400–1000 nm (Figure S8, Supporting Information). In the spectrum recorded at t = 30 min an intense absorption peak ($A_{max}$~ 1.4) appeared at 400 nm, which was associated with the LSPR of the spherical AgNPs.[35] At t = 60 and 120 min the LSPR had a broader band, which agreed with: the increase in AgNPs size; the broadening of the distribution recorded (Figure S6, Supporting Information); the increase of the surface coverage (Figure S6f, Supporting Information) and the interparticle coupling.[40] At t = 240 and 360 min, a further broadening of the LSPR peaks was observed with an absorbance value over the whole wavelength range (400–900 nm) of roughly 1.2 and 1.1. The higher absorbance value for the sample synthesized after 240 min compared to the 360 min could be explained by the lower reflectance (Figure S7c, Supporting Information).

The synthesized BL/PPTL nanocomposites were then tested in photothermal conversion upon irradiation with visible light by simulating the sunlight radiation, with a power density of 100 mW $cm^{-2}$ (1 Sun) in air and using a thermocamera (Figure 1e–g).

All the photothermal profiles showed an increase in temperature over time well-fitted with an asymptotic exponential trend ($R^2$ = 0.99) as reported in Figure S9a–e (Supporting Information). The trend of the maximum ΔT (°C) vs decoration times reached the maximum value in the BL/PPTL samples decorated for 240 min with AgNPs (ΔT ~ 14.6 ± 0.3 °C after 7 s of irradiation, N samples = 3). This decoration also showed the highest temperature gradient upon illumination (Figure S9f, Supporting Information) (7.3 ± 0.4 °C/s for t = 0s, N samples = 3).

For completeness, the photothermal properties of such BL/PPTL layer were also evaluated at other sunlight power densities (i.e., 0.5 and 1.5 Sun) (Figure 1h; Figure S10, Supporting Information) and under IR laser irradiation at 808 nm at high power density (1586 mW $cm^{-2}$) (Figure S11, Supporting Information). Under laser irradiation, the surface temperature reached the value of 208.2 ± 0,6 °C (N sample = 3) in 7 s. Interestingly the reached value was higher than the one obtained using a PDMS layer with a similar thickness (66 µm) and covered with graphene (one of the most exploited materials for photothermal actuation) and AuNPs as photothermal enhancers i.e., ≈150 °C under an IR laser (808 nm) and a similar irradiation power (3000 mW $cm^{-2}$).[24]

The photothermal conversion efficiency (PCE, $\eta$) was calculated by adapting the methods used in liquid-NPs solutions[44] to thin films suspended in air (Section S3, Supporting Information).

The PCE results for single wavelength laser source and broad solar spectrum agreed: 41.7% and 40.8%, respectively.

We tested the adhesion properties of AgNPs formed on PDMS in a 20 mM AgF ethanolic solution for 240 min (Figure S12, Supporting Information). The reflectance spectra recorded before and after the adhesion test were identical confirming the high adhesion between the PDMS and AgNPs.

Differently from the conventional premixing of photothermal agents (e.g., CNT),[45] the in situ synthesis of AgNPs onto the PDMS surface did not change significantly mechanical properties. Young's Modulus of PDMS and PDMS/AgNPs (240 min synthesis) were not statistically different being 2.55 ± 0.52 MPa and 1.95 ± 0.34 MPa, respectively.

For the above-mentioned reason, the BL/PPTL sample decorated for 240 min with AgNPs was used for the subsequent development of the photothermal-hygroscopic actuator.

We designed the BL/PPTL/HL actuator (**Figure 2**a), taking inspiration from the morphometric structure of the Geraniaceae seeds (i.e., *Pelargonium appendiculatum*) (Figure 2b–d). These seeds are characterized by a central body, the awn, which shows hygroscopic actuation to promote spreading, soil penetration, and germination. As shown in the section view of the awn (Figure 2c,d), the structure can be decomposed as an effective bilayer, with an oriented and parallel cellulose distribution, as hygroscopic layer, and a lignin-based layer.[7]

To guarantee adhesion between hydrophobic PDMS/AgNPs substrate and hydrophilic cellulose layer, we used air plasma

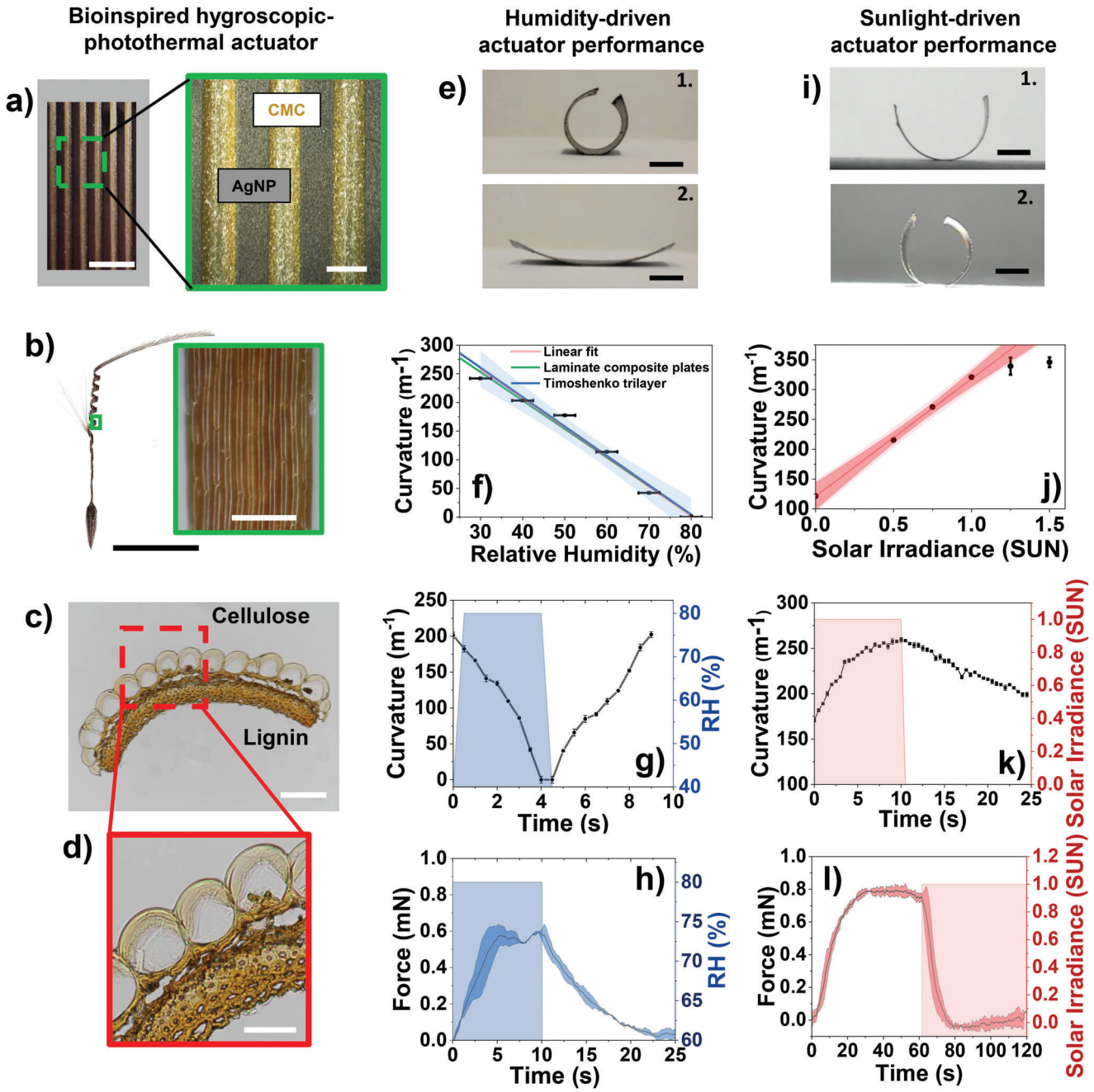


**Figure 2.** a) Picture of the BL/PPTL/HL actuator showing the AgNPs region (brown, BL/PPTL) and printed, aligned, and parallel CMC tracks (yellow tracks, HL). Scale bar is 0.5 cm. The inset shows a zoom from (a). Scale bar is 1 mm. b) Picture of a *Pelargonium appendiculatum* seed. Scale bar is 1 cm. The inset shows the microfibrils cellulose structure. Scalebar is 200 µm. c) White image of a transversal section of the awn in the cellulose- and lignin-based regions. Scalebar is 100 µm. d) Zoom from (c) showing the cellulose-based region. Scale bar is 50 µm. e) Pictures of the BL/PPTL/HL actuator exposed to relative humidity (%RH) equal to 30% (1) and 80% (2). f) Curvature of the actuator vs relative humidity (30%–80%). Data are fitted by linear regression and in good agreement with the laminate composite plates model and the Timoshenko trilayer model. g) Curvature of the actuator vs time (s) with %RH changing from 40% to 80% (average %RSD = 2.7%, N sample = 3). h) Forces (mN) vs time (s) with %RH changing from 40% to 80%. i) Pictures of the actuator exposed to 0 Sun (1) and 1 Sun (2) at a fixed %RH = 60%. j) Curvature variation of the actuator vs time (s) exposed to 0–1.5 Sun at a fixed %RH = 60%. k) Curvature variation of the actuator vs time (s) exposed to 1 Sun (average %RSD = 0.7%, N sample = 3). l) Force (mN) vs time (s) of the actuator exposed to 1 Sun at a fixed %RH = 60%. In f-h and j-l data are provided as average values over 3 replicates with error bars representing one standard deviation.

followed by the nanometric coating with PVA, as described in the protocol reported in.[46] The combined plasma oxidation and PVA treatment have been reported to be long-term stable, ensuring long-term hydrophilicity of the PDMS surfaces in contrast to the only plasma oxidized PDMS, which tends to regain its surface hydrophobicity 1 day after treatment. The increase in hydrophilicity was confirmed by the contact angle analysis reported in Figure S13 (Supporting Information). Figure S14 (Supporting Information) shows the thickness of the PVA coating (≈60 nm) on the blank PDMS layer. Such values agree with those reported in the literature for similar spin coating protocols.[47]

SEM EDX analysis reported in Figure S5 (Supporting Information), for the AgNPs synthesis of 240 min before and after the use of air plasma shows the O% weight increases from 11.26 ± 0.58% to 11.87 ± 0.10% (N = 3). However, this increase could not be considered statistically significant (Student's t-test confidence level = 95%). Also, the temperature variations (ΔT,°C) over time (s) under sunlight exposure (1 Sun) did not show a significant variation of the photothermal properties due to the air plasma (Figure S15, Supporting Information).

Based on the mechanical characterization of the materials, PDMS/AgNPs and CMC (Figure S16, Supporting Information), we designed the CMC layer (considering an equivalent thickness, obtained by averaging the CMC tracks thickness and the inter-track distances) to predict the curvature and so, to properly design the actuator (Figures S17–S19, Supporting Information). To this purpose, we considered both Timoshenko beam model, and the laminate composite plates model (Section S4, Supporting Information).[38] In particular, we consider the actuator as a trilayered structure, in which the PDMS/AgNPs passive substrate is stacked with a PVA buffer layer, and the hygroscopic CMC layer is deposited on the topmost part.

CMC hydrogel (10% in deionized water) was printed via DIW (Video S1, Supporting Information) on the activated PDMS/AgNPs surface and totally dried in the oven to obtain a pattern of CMC tracks wide 0.91 ± 0.06 mm (N samples = 6), distanced 0.67 ± 0.02 mm (N samples = 6) (Figure 2a; Figure S20, Supporting Information) and thick 20.8 ± 2.1 μm (N samples = 6) (Figure S21, Supporting Information). Accordingly, with the Section S4 (Supporting Information), an equivalent thickness equal to 13.5 ± 2.5 μm was calculated.

We tested the adhesion properties of CMC on PDMS/AgNPs surface (Figure S22, Supporting Information). The surficial microscopy images captured after the adhesion test proved the integrity of the CMC tracks and the good adhesion between the PDMS/AgNPs and CMC mediated by PVA (Figure S22, Supporting Information).

Considering the key role played by hygroscopic actuation in the proposed multi-physics-driven system, we preliminarily characterized the actuator response versus RH only.

We first addressed the hygromorphic behavior of the considered actuator regarding both its kinematics (curvature) and statics (force) performance as a function of %RH. When the environmental %RH decreased, it induced a contraction of the CMC tracks, thus increasing actuator curvature (positive curvature intended as the folding of the hygroscopic layer) (Figure 2e.1); reciprocally, a decrease in %RH caused a reduction in the actuator curvature, i.e., to unbend (Figure 2e.2), as reported in Video S2 (Supporting Information).

Considering that, at least at a first approximation, the curvature of a thin multilayer (plate) can be modeled regardless of sample width (w) and length (l),[48] so that actuation force is consequently computed per unit width,[10] we fixed the geometrical dimensions of the rectangular sample actuator as w = 1 cm and l = 2 cm.

We characterized the curvature response in a climatic chamber (Figure 2f). From the recorded data, we also extracted the humidity value $\Phi_0 = 80\%$ associated with null curvature, to be used for model calibration (Section S4, Supporting Information). Both laminate composite plates and Timoshenko model predicted the curvature response within 95% confidence interval. These results highlighted that we can accurately control the actuator curvature based on RH.

We then proceeded to analyze the time response of the hygroscopic actuator. Considering that water adsorption in the cellulose layer was driven by diffusion,[10,15] we first characterized the time evolution of the curvature by increasing the humidity level (step increase from 40% to 80%) using deionized water aerosol (i.e., working conditions over the diffusion limit).

Figure 2g shows the time behavior of the actuator subjected to an RH stepwise function. During water adsorption, the structure decreased its curvature from $\kappa = 2.01 \pm 0.15$ to $\kappa = 0 \pm 0.12\ \mathrm{cm}^{-1}$ in $\tau_{RH} = 4.11 \pm 0.23$. Moreover, considering that the actuation was mediated by Fickian diffusion upon the cellulose layer, the diffusivity of the CMC layer could be evaluated as $D_{CMC} \approx h_{CMC}^2/\tau_{RH} = 2.94 \pm 0.34 \times 10^{-11}\mathrm{m}^2\mathrm{s}^{-1}$.

Figure 2h reports the force produced by the hygroscopic actuation (under quasi-static conditions) by varying the humidity level from RH = 60% to RH = 80%, with the maximum force equal to $F_{RH} = 0.57 \pm 0.07$ mN. The considered force was predicted by both the Timoshenko model ($F_T = 0.58$ mN) and the laminate composite plates model ($F_{LC} = 0.56$ mN) within a confidence interval of 95% (Figures S23 and S24, Supporting Information). The force estimate turned out to be in good agreement with the experimental results (thus corroborating the working assumptions introduced for ease of model derivation (Section S4, Supporting Information, Equations S7 and S8).

Thanks to the photothermal effect, we promoted water desorption by increasing the substrate temperature with a broad solar spectrum with 1 Sun power density. Considering water adsorption enthalpy, an increase in temperature at constant environmental RH led to a bending of the actuator (Figure 2i and Video S2, Supporting Information). An increase in temperature determined an increase in the rate of humidity desorption and so, the localized amount of humidity in the cellulose layer was consequently reduced.

At first approximation, the solar irradiance and humidity could be analyzed as independent variables. We characterized the kinematics and statics of the actuator by varying the optical power density (0.5–1.5 Sun) at a fixed initial (RH = 60%) humidity level (Figure 2j). The curvature shows a linear trend ($R^2 = 0.99$) up to 1 Sun of solar irradiance, above that curvature saturation occurs. Based on the previous characterization results on purely hygroscopic actuation, the residual RH was < 20% on the cellulose layer for solar irradiance > 1 Sun.

Figure 2k shows the response of the load-free actuator driven at 1 Sun (step application of the solar irradiance). Here, we can observe the combined effect of photothermal conversion and water desorption. The actuator changed its curvature from $\kappa = 1.71 \pm 0.05$ to $\kappa = 2.54 \pm 0.03\ \mathrm{cm}^{-1}$ in $t_{Sun} = 6.8 \pm 0.3$ s.

Figure S25 (Supporting Information) illustrates actuation performance retention over 100 cycles of irradiation: bending curvature changed by only 5% in not irradiation conditions and roughly 0.5% under 1 Sun irradiation, respectively.

In Figure 2l we finally analyzed the static performance when the actuator was irradiated with a stepwise function from 0 to 1 Sun, reaching a maximum force of $F_{Sun} = 0.76 \pm 0.02$ mN. Interestingly, the corresponding force (≈1 mN) was associated to a moment (≈$10^{-5}$ N m) in the same order of magnitude to those of Geraniaceae seeds (e.g., *Pelargonium appendiculatum* and *Erodium malacoides*), as reported in Figure S26 (Supporting Information).

To illustrate the potential for application of the proposed BL/PPTL/HL actuator, while keeping implementation efforts in line with the present developmental stage, we introduced several sunlight-driven demonstrators, namely grasper, crawler, coiler/roller, weightlifter, and a final reconfiguration obtained by implementing an actuator devised for uniaxial programmed motion responsive to sunlight (**Figure 3**).

The BL/PPTL/HL actuator (2 cm × 1 cm × 0.006 cm, mass 13.9 ± 0.9 mg, N samples = 6) could act as a wireless soft grasper (Figure S27a, Supporting Information). The soft grasper is shown in Figure 3a and Video S3 (Supporting Information). With light exposure (1 Sun), the bilayer bent to grip a cargo with size (14 cm × 1.70 cm × 0.75 cm, mass 156 mg). When the light was turned off the cargo was released. In the reported test, the grasper handled a cargo with a mass greater than 11-fold its mass (and a volume greater than ≈1500-fold its volume).

A crawler demonstrator (with the same embodiment of the previous grasper) is shown in Figure 3b and Video S4 (Supporting Information). Locomotion was driven by cyclic irradiance, leading to cyclic contraction/extension of the crawler structure (it contracted under sunlight actuation, and stretched back upon irradiation removal). A constant unidirectional movement was obtained thanks to the different friction forces between the two ends of the actuator, modified with 5 iron threads in front (bent at 110 °) and 5 behind (straight), respectively. The proposed crawler moves at ≈1 BL $min^{-1}$ considering the experimental variation of irradiance as function of time. Considering the driving illumination, the crawler moves at 0.3 BL $Sun^{-1}$ cycle.

Lifting tests on such demonstrators were also reported using payloads of 42.6 and 144.1 mg (≈3 and 10-fold the actuator mass) (Video S5, Supporting Information). Under sunlight exposure, the actuator could lift the 42.6 mg payload of 4 mm (work ≈1.7 μJ) and the 144.1 mg payload of 2 mm (work ≈2.8 μJ), corresponding to an energy density of 0.14 and 0.23 kJ $m^{-3}$, respectively.

A demonstrator capable of coiling/uncoiling (4.5 cm × 0.5 cm × 0.006 cm) (Figure 3d) was also implemented (Video S6, Supporting Information), by laying the CMC tracks at a 20° angle with respect to the actuator longitudinal axes (Figure S27b–d, Supporting Information), similarly to the tilt and microfibril angle (MFA) in Geraniaceae seed structures.[8] Such a demonstrator could also be used to implement rolling motions: we obtained an average rolling speed of 0.4 mm $s^{-1}$ upon 2 locomotion cycles (Figure 3e and Video S6, Supporting Information), yet further investigations on helical radius reduction and boundary conditions to trigger rolling upon coiling are necessary to design rolling systems with enhanced performance.

Taking advantage of the possibility of printing the tracks in different directions on the same BL/PPTL, we have also designed and fabricated a reconfigurable structure devised for uniaxial programmed motion (Figure 3f,g), recalling the uniaxial opening/closing motion of some flowers (e.g., *Carlina aucalis*),[49] and using the design shown in Figure S27e (Supporting Information).

When exposed to 1 Sun, the considered structure reconfigured its shape in nearly 7 s (Video S7, Supporting Information), and the starting configuration was recovered upon removing the solar stimulus. The dynamic temperature profile caused by irradiation further elucidated the photothermal-hygroscopic actuation strategy introduced in the present demonstrator (Figure 3g.4 and Video S7, Supporting Information).

Overall, and commensurate with the present developmental stage, the reported demonstrators support the potential for effective implementation of the proposed photothermal-hygroscopic actuation strategy in a variety of applications involving soft material systems, and in particular soft actuators.

## 3. Conclusion

A bioinspired plasmonic photothermal-hygroscopic nanocomposite with AgNPs integrated onto a PDMS surface is here designed and fabricated for the creation of a sunlight-driven (1 Sun) actuator.

An actuator activated by the combination of sunlight and moisture offers a concrete original contribution to the growing quest for actuation systems driven by renewable energy sources, paving the way to develop next-generation soft materials/robotics systems at a sustainable cost.

Thanks to the in situ synthesis, the proposed photothermal-hygroscopic actuators can be obtained through facile fabrication steps involving commonly available materials in the market (e.g., PDMS and AgF for the photothermal effect) and in nature (e.g., cellulose-based materials).

The actuator shows reversible deformation and curvature changes featuring a ≈6.8 ± 0.3 s response time, associated with a ≈43% change in curvature and a 0.76 ± 0.02 mN force under 1 Sun irradiation.

The approach enables a versatile and simple strategy for fabricating soft actuators with more complex designs (grasper, crawler, coiler, lifter, and a light-responsive actuator structure devised for programmed motion) activated by sunlight power.

Compared to the current state of the art in sunlight driven photothermal-humidity actuators, in this work we couple an: 1) in situ, one-step and high-yield synthesis of the plasmonic photothermal agent onto the inactive layer of the actuator with a deep photothermal characterization; 2) anisotropic actuation obtained through controlled alignment of the cellulose tracks printed and aligned similarly *Pelargonium appendiculatum* seed structures; 3) analysis of statics and kinematics properties of the actuation coupled with modeling.

This work provides a useful way for developing a new generation of plasmonic soft actuators for sunlight-driven bioinspired and sustainable soft microrobots actuated by renewable energy sources.

The reported actuator is based on PDMS (as hosting material) that is one of the most used silicon-based elastomers in soft

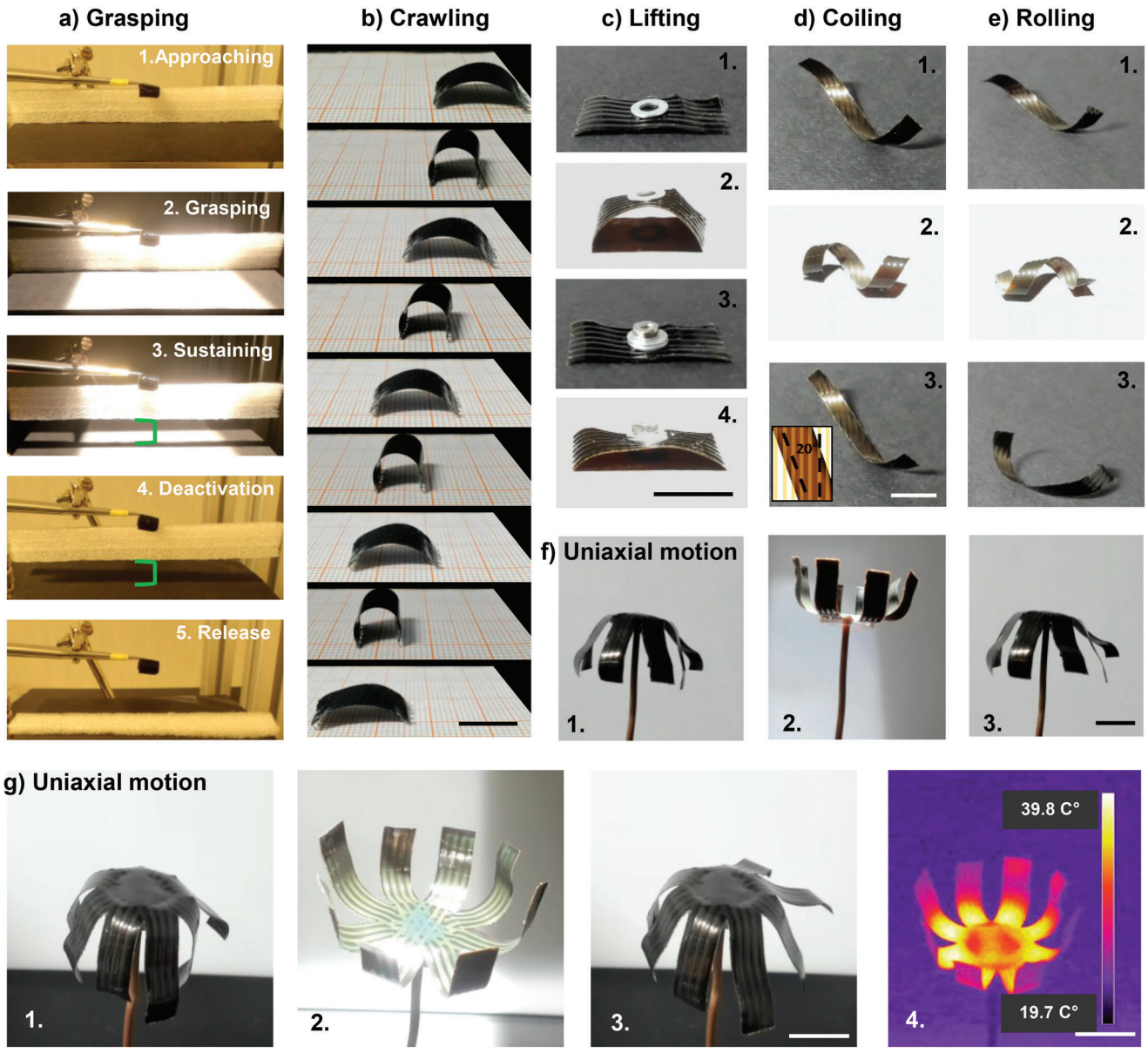


**Figure 3.** a) Grasping test of a polystyrene sample (156 mg mass ~ 11-fold the actuator mass) with a BL/PPTL/HL rectangular actuator (2 × 1 cm). The test consists of: 1. Approaching; 2. Grasp activation under light exposure; 3. Sustained grasping; 4. Grasp deactivation; 5. Sample release. b) Crawling test of the rectangular BL/PPTL/HL actuator (2 × 1 cm) under subsequent light exposure. Scale bar is 2 cm. c) Lifting tests of metallic nuts and washers i.e., 42.6 and 144.1 mg (3-fold and 10-fold the actuator mass, respectively) using a rectangular BL/PPTL/HL actuator (2 × 1 cm). 1 and 2 show the lifting of the 42.6 mg sample under light exposure while 3 and 4 show the 144.1 mg one. d) Coiling test of a rectangular actuator (0.5 × 4.5 cm) with CMC tracks printed with an angle of 20° with respect to the longitudinal axis. The pictures show a dark(1)/light exposure(2)/dark(3) cycle. Scale bar is 1 cm. e) Rolling test of the rectangular actuator reported in (d) under dark(1)/light exposure(2)/dark(3) cycles. Scale bar is the same as (d). f,g) Artificial light-responsive actuator structure devised for uniaxial programmed motion based on the BL/PPTL/HL in lateral (f) and tilted view (g) exposed to a dark(1)/light exposure(2)/dark(3) cycle. Scalebar is 1 cm. (4) Thermocamera image during the exposure of the actuator structure devised for uniaxial programmed motion under sunlight. Scale bar is 1 cm. All the experiments are performed under a simulated sunlight power density of 1 Sun.

robotics.[50] However, the reported fabrication process could be extended to other composites, in which the PDMS layer could be exploited as a coating or hosting material for flat or fibrous reinforcing polymers,[51] paving the way for a multi-material approach with wider flexibility for soft robotics applications.

A proof of concept of the employment as coating material for deformable structure (i.e., Kapton tape, Polyimide) with a relatively high Young's modulus (2.5 GPa, Figure S28, Supporting Information)[52] is reported in Video S8 (Supporting Information). The multi-layered composite was reversibly actuated by sunlight with a power density of 1 Sun.

Moreover, based on further calibration of the hygroscopic-photothermal response of the plasmonic nanocomposite, additional applications for sensing could be envisaged. For

instance, considering the self-folding of 2D PDMS-based materials in origami/kirigami 3D structures,[53] the proposed technology could open new horizons in the fabrication of 3D soft actuators/robots driven by sunlight.

In perspective, the proposed plasmonic nanocomposite technology could be used to actuate also miniature medical end-effectors based on low-intensity (e.g., endoscopic) irradiation, thus complementing the relatively more widespread use of high-intensity laser irradiation in medical applications, such as, e.g., thermal therapy.[54] Finally, the proposed technology could be used to also develop energy harvesting applications based on photomechanical effects[55] stimulated by daily environmental variations, as well as bioinspired systems for environmental exploration, including, e.g., artificial seeds able to adaptively explore soils.[56]

## Supporting Information

Supporting Information is available from the Wiley Online Library or from the author.

## Acknowledgements

S.M. and L.C. contributed equally to this work. This work had received funding from the European Union Horizon 2020 research and innovation programme under grant agreement No 101017940 (I-Seed), and from the Israeli Ministry of Science and Technology (MOST) Joint Laboratory Israel-Italy (A Plant-Inspired Robot Emulating Decision-Making Abilites of Plants in Dynamical Environments).

Open Access Funding provided by Istituto Italiano di Tecnologia within the CRUI-CARE Agreement.

## Conflict of Interest

The authors declare no conflict of interest.

## Data Availability Statement

The data that support the findings of this study are available from the corresponding author upon reasonable request.

## Keywords

bioinspired and sustainable soft robotics, hygroscopic actuations, photothermal effects, plasmonic nanocomposites, sunlight actuations

Received: April 1, 2023
Published online:

[1] B. Mazzolai, C. Laschi, *Sci Robot* **2020**, *5*, eaba6893.
[2] F. Hartmann, M. Baumgartner, M. Kaltenbrunner, *Adv. Mater.* **2021**, *33*, 2004413.
[3] C. A. Aubin, B. Gorissen, E. Milana, P. R. Buskohl, N. Lazarus, G. A. Slipher, C. Keplinger, J. Bongard, F. Iida, J. A. Lewis, R. F. Shepherd, *Nature* **2022**, *602*, 393.
[4] S. Poppinga, C. Zollfrank, O. Prucker, J. Rühe, A. Menges, T. Cheng, T. Speck, *Adv. Mater.* **2018**, *30*, 1703653.
[5] C. Dawson, J. F. V Vincent, A.-M. Rocca, *Nature* **1997**, *390*, 668.
[6] C. J. Eger, M. Horstmann, S. Poppinga, R. Sachse, R. Thierer, N. Nestle, B. Bruchmann, T. Speck, M. Bischoff, J. Rühe, *Adv. Sci.* **2022**, *9*, 2200458.
[7] R. Elbaum, L. Zaltzman, I. Burgert, P. Fratzl, *Science* **2007**, *316*, 884.
[8] Abraham, R. Elbaum, *New Phytol.* **2013**, *199*, 584.
[9] H. S. Atamian, N. M. Creux, E. A. Brown, A. G. Garner, B. K. Blackman, S. L. Harmer, *Science* **2016**, *353*, 587.
[10] S. Taccola, F. Greco, E. Sinibaldi, A. Mondini, B. Mazzolai, V. Mattoli, *Adv. Mater.* **2015**, *27*, 1668.
[11] B. Shin, J. Ha, M. Lee, K. Park, G. H. Park, T. H. Choi, K.-J. Cho, H.-Y. Kim, *Sci Robot* **2018**, *3*, eaar2629.
[12] H. Cheng, Y. Hu, F. Zhao, Z. Dong, Y. Wang, N. Chen, Z. Zhang, L. Qu, *Adv. Mater.* **2014**, *26*, 2909.
[13] D. Van Opdenbosch, G. Fritz-Popovski, W. Wagermaier, O. Paris, C. Zollfrank, *Adv. Mater.* **2016**, *28*, 5235.
[14] F. Zhang, M. Yang, X. Xu, X. Liu, H. Liu, L. Jiang, S. Wang, *Nat. Mater.* **2022**, *21*, 1357.
[15] D. Lunni, M. Cianchetti, C. Filippeschi, E. Sinibaldi, B. Mazzolai, *Adv. Mater. Interfaces* **2020**, *7*, 1901310.
[16] X. Pang, J. Lv, C. Zhu, L. Qin, Y. Yu, *Adv. Mater.* **2019**, *31*, 1904224.
[17] J. Hong, C. Xu, B. Deng, Y. Gao, X. Zhu, X. Zhang, Y. Zhang, *Adv. Sci.* **2022**, *9*, 2103926.
[18] B. Han, Y.-L. Zhang, Q.-D. Chen, H.-B. Sun, *Adv. Funct. Mater.* **2018**, *28*, 1802235.
[19] G. Cai, J. H. Ciou, Y. Liu, Y. Jiang, P. S. Lee, *Sci. Adv.* **2019**, *5*, aaw7956.
[20] Y. Hu, L. Yang, Q. Yan, Q. Ji, L. Chang, C. Zhang, J. Yan, R. Wang, L. Zhang, G. Wu, J. Sun, B. Zi, W. Chen, Y. Wu, *ACS Nano* **2021**, *15*, 5294.
[21] Y. Li, J. Wang, L. Huang, L. Chen, H. Gao, Y. Ni, Q. Zheng, *ACS Sustainable Chem. Eng.* **2022**, *10*, 6414.
[22] H. Zhao, X. Qi, Y. Ma, X. Sun, X. Liu, X. Zhang, M. Tian, L. Qu, *Nano Lett.*. **2021**, *21*, 8126.
[23] D. D. Han, Y. L. Zhang, H. B. Jiang, H. Xia, J. Feng, Q. D. Chen, H. L. Xu, H. B. Sun, *Adv. Mater.* **2015**, *27*, 332.
[24] Y. Yang, Y. Liu, Y. Shen, *Adv. Funct. Mater.* **2020**, *30*, 1910172.
[25] Duan, F. Liu, Y. Kong, M. Hao, J. He, J. Wang, S. Wang, H. Liu, Y. Sang, ACS Appl, *Nano Mater.* **2020**, *3*, 1002.
[26] Hu, J. Liu, L. Chang, L. Yang, A. Xu, K. Qi, P. Lu, G. Wu, W. Chen, Y. Wu, *Adv. Funct. Mater.* **2017**, *27*, 1704388.
[27] A. Mourran, H. Zhang, R. Vinokur, M. Möller, *Adv. Mater.* **2017**, *29*, 1604825.
[28] H. Qin, T. Zhang, N. Li, H.-P. Cong, S.-H. Yu, *Nat. Commun.* **2019**, *10*, 2202.
[29] J. Chen, J. Feng, F. Yang, R. Aleisa, Q. Zhang, Y. Yin, *Angew. Chem., Int. Ed.* **2019**, *58*, 9275.
[30] F. Meder, G. A. Naselli, A. Sadeghi, B. Mazzolai, *Adv. Mater.* **2019**, *31*, 1905671.
[31] Y. Wang, E. Sachyani Keneth, A. Kamyshny, G. Scalet, F. Auricchio, S. Magdassi, *Adv. Mater. Technol.* **2022**, *7*, 2101058.
[32] Z. Li, Z. Ye, L. Han, Q. Fan, C. Wu, D. Ding, H. L. Xin, N. V. Myung, Y. Yin, *Adv. Mater.* **2021**, *33*, 2006367.
[33] Z. Xie, Y. Duo, Z. Lin, T. Fan, C. Xing, L. Yu, R. Wang, M. Qiu, Y. Zhang, Y. Zhao, X. Yan, H. Zhang, *Adv. Sci.* **2020**, *7*, 1902236.
[34] B. Yang, C. Li, Z. Wang, Q. Dai, *Adv. Mater.* **2022**, *34*, 2107351.
[35] S. Mariani, A. A. La Mattina, A. Paghi, L. Strambini, G. Barillaro, *Adv. Funct. Mater.* **2021**, *31*, 2100774.
[36] S. Mariani, M. Corsi, A. Paghi, A. A. La Mattina, L. Strambini, F. P. Frontini, G. Di Giuseppe, G. Barillaro, *Adv. Opt. Mater.* **2021**, *10*, 2101610.
[37] A. K. Jaiswal, A. Hokkanen, M. Kapulainen, A. Khakalo, Nonappa, O. Ikkala, H. Orelma, *ACS Appl. Mater. Interfaces* **2022**, *14*, 3315.
[38] B. Shapiro, E. Smela, *J Intell Mater Syst Struct* **2006**, *18*, 181.
[39] https://nanocomposix.com/pages/silver-nanoparticles-optical-properties.

[40] P. Merkl, S. Zhou, A. Zaganiaris, M. Shahata, A. Eleftheraki, T. Thersleff, G. A. Sotiriou, ACS Appl, *Nano Mater.* **2021**, *4*, 5330.
[41] N. Kwon, H. Oh, R. Kim, A. Sinha, J. Kim, J. Shin, J. W. M. Chon, B. Lim, *Nano Lett.* **2018**, *18*, 5927.
[42] Q. Zhang, J.-J. Xu, Y. Liu, H.-Y. Chen, *Lab Chip* **2008**, *8*, 352.
[43] S.-U. Victor, V.-B. J. Roberto, in *Silver Nanoparticles* (Ed.: K. Maaz), IntechOpen, Rijeka, **2018**, p. 147, Ch. 8.
[44] H. Breitenborn, J. Dong, R. Piccoli, A. Bruhacs, L. V. Besteiro, A. Skripka, Z. M. Wang, A. O. Govorov, L. Razzari, F. Vetrone, R. Naccache, R. Morandotti, *APL Photonics* **2019**, *4*, 126106.
[45] J. H. Kim, J.-Y. Hwang, H. R. Hwang, H. S. Kim, J. H. Lee, J.-W. Seo, U. S. Shin, S.-H. Lee, *Sci. Rep.* **2018**, *8*, 1375.
[46] T. Trantidou, Y. Elani, E. Parsons, O. Ces, *Microsyst. Nanoeng.*. **2017**, *3*, 16091.
[47] C. Li, Q. Li, L. Sun, X. Ye, S. Chen, Z. Wu, J. Huang, W. Wu, X. Jiang, *Opt. Express* **2018**, *26*, 19707.
[48] S. Timoshenko, *Theory of Plates and Shells*, McGraw Hill, New York **1959**.
[49] Y. Tahouni, F. Krüger, S. Poppinga, D. Wood, M. Pfaff, J. Rühe, T. Speck, A. Menges, *Bioinspir. Biomim.* **2021**, *16*, 055002.
[50] E. Sachyani Keneth, A. Kamyshny, M. Totaro, L. Beccai, S. Magdassi, *Adv. Mater.* **2021**, *33*, 2003387.
[51] R. Ariati, F. Sales, A. Souza, R. A. Lima, J. Ribeiro, *Polymers (Basel)*. **2021**, *13*, 4258.
[52] https://www.mit.edu/~6.777/matprops/polyimide.htm.
[53] T. van Manen, S. Janbaz, M. Ganjian, A. A. Zadpoor, *Mater. Today* **2020**, *32*, 59.
[54] E. Redolfi Riva, A. Desii, E. Sinibaldi, G. Ciofani, V. Piazza, B. Mazzolai, V. Mattoli, *ACS Nano* **2014**, *8*, 5552.
[55] Y.-X. Shi, W.-H. Zhang, B. F. Abrahams, P. Braunstein, J.-P. Lang, *Angew. Chem., Int. Ed.* **2019**, *58*, 9453.
[56] L. Cecchini, S. Mariani, M. Ronzan, A. Mondini, N. M. Pugno, B. Mazzolai, *Adv. Sci.* **2023**, *10*, 2205146.